ISSN 1674-1056
http://cpb.iphy.ac.cn
http://iopscience.iop.org/cpb
中国物理 B
Chinese Physics
中国物理 Chinese Physics B

Hydrodynamic binary coalescence of droplets under air flow in a hydrophobic microchannel

Chao Wang(王超), Chao-qun Shen(沈超群), Su-chen Wu(吴苏晨), Xiang-dong Liu(刘向东), Fang-ping Tang(汤方平)

Citation: Chin. Phys. B . 2019, 28(2): 024702. **doi:** 10.1088/1674-1056/28/2/024702
Journal homepage: http://cpb.iphy.ac.cn; http://iopscience.iop.org/cpb

What follows is a list of articles you may be interested in

Walking of spider on water surface studied from its leg shadows

Yelong Zheng(郑叶龙), Hongyu Lu(鲁鸿宇), Jile Jiang(蒋继乐), Dashuai Tao(陶大帅), Wei Yin(尹维), Yu Tian(田煜)

Chin. Phys. B . 2018, 27(8): 084702. **doi:** 10.1088/1674-1056/27/8/084702

Molecular dynamics simulations of the nano-droplet impact process on hydrophobic surfaces

Hu Hai-Bao, Chen Li-Bin, Bao Lu-Yao, Huang Su-He

Chin. Phys. B . 2014, 23(7): 074702. **doi:** 10.1088/1674-1056/23/7/074702

Simultaneous effects of magnetic field and space porosity on compressible Maxwell fluid transport induced by a surface acoustic wave in a microchannel

Khaled S. Mekheimer, Soliman R. Komy, Sara I. Abdelsalam

Chin. Phys. B . 2013, 22(12): 124702. **doi:** 10.1088/1674-1056/22/12/124702

Multi-relaxation time lattice Boltzmann simulation of inertial secondary flow in a curved microchannel

Sun Dong-Ke, Xiang Nan, Jiang Di, Chen Ke, Yi Hong, Ni Zhong-Hua

Chin. Phys. B . 2013, 22(11): 114704. **doi:** 10.1088/1674-1056/22/11/114704

Droplet impact on regular micro-grooved surfaces

Hu Hai-Bao, Huang Su-He, Chen Li-Bin

Chin. Phys. B . 2013, 22(8): 084702. **doi:** 10.1088/1674-1056/22/8/084702

Hydrodynamic binary coalescence of droplets under air flow in a hydrophobic microchannel*

Chao Wang(王超)[1], Chao-qun Shen(沈超群)[1], Su-chen Wu(吴苏晨)[2], Xiang-dong Liu(刘向东)[1,†], and Fang-ping Tang(汤方平)[1]

[1] *School of Hydraulic, Energy and Power Engineering, Yangzhou University, Yangzhou* 225127, *China*
[2] *Key Laboratory of Energy Thermal Conversion and Control of Ministry of Education, School of Energy and Environment, Southeast University, Nanjing* 210096, *China*

(Received 13 July 2018; revised manuscript received 25 October 2018; published online 10 January 2019)

Based on the volume of fluid (VOF) method, we conduct a numerical simulation to study the hydrodynamic binary coalescence of droplets under air flow in a hydrophobic rectangular microchannel. Two distinct regimes, coalescence followed by sliding motion and that followed by detaching motion, are identified and discussed. Additionally, the detailed hydrodynamic information behind the binary coalescence is provided, based on which a dynamic mechanical analysis is conducted to reveal the hydrodynamic mechanisms underlying these two regimes. The simulation results indicate that the sliding motion of droplets is driven by the drag force and restrained by the adhesion force induced by the interfacial tension along the main flow direction. The detachment (*i.e.*, upward motion) of the droplet is driven by the lift force associated with an aerodynamic lifting pressure difference imposed on the coalescent droplet, and also restrained by the adhesion force perpendicular to the main flow direction. Especially, the lift force is mainly induced by an aerodynamic lifting pressure difference imposed on the coalescent droplet. Two typical regimes can be quantitatively recognized by a regime diagram depending on Re and We. The higher Re and We respectively lead to relatively larger lift forces and smaller adhesion forces acting on the droplet, both of which are helpful to detachment of the coalesced droplet.

Keywords: droplet, coalescence, sliding, detachment, microchannel

PACS: 47.55.df, 47.55.np, 68.03.–g, 68.08.–p **DOI:** 10.1088/1674-1056/28/2/024702

1. Introduction

The dynamic behavior of droplets driven under air flow on the substrate of microchannel, including deformation, movement, coalescence, detachment, and breakup,[1,2] are omnipresent in real applications, such as phase extraction,[3] oil recovery,[4] the removal of grease in detergency,[5,6] and water management in proton exchange membrane fuel cell (PEMFC).[7–9] In particular, the coalescence of droplets and the following dynamic behaviors of the coalescent droplet, during which the morphology and area of the interface as well as the mixing strength change obviously, play an important role in the performance of the real applications. For example, in the water management of the PEMFC, droplet coalescence and the following behaviors (such as sliding and detaching) under the external flow are the typical phenomena during the removal of water in the cathode flow microchannel,[10] which have an obvious influence on efficiency and lifetime of the PEMFC. Therefore, the investigation of the hydrodynamics underlying the droplet coalescence and the following behavior in a microchannel under the external flow is significant for understanding and optimizing the above-mentioned real processes.

Up to now, several experiments based on high-speed visualization systems have been conducted to intuitively observe the dynamic behavior of a single droplet on the substrate in a microchannel under imposed shear or convection.[11–15] The effects of confinement,[13,16] microchannel shape,[14,17] flow rate,[18] droplet volume,[12] and droplet viscosity[19] on the dynamic behavior have been investigated. It has been demonstrated by Vananroye *et al.*[13,19] that a single droplet with a given size is able to detach from the substrate of the microchannel if the capillary number of gas flow reaches a critical value which depends on the confinement degree of the microchannel. Akhtar *et al.*[14] found that a tapered microchannel is beneficial for droplets to detach from the microchannel substrate because gas flow velocity increases along the tapering geometry. Furthermore, they demonstrated that the use of a hydrophilic gas diffusion layer is able to enhance the effect of the tapering microchannel on the droplet exhausting. In addition, it was also proved that decreasing the viscosity and volume of the droplet contributes to droplet sliding and detaching in a microchannel.[15]

Apart from experimental investigations, theoretical analysis and numerical simulations have also been performed to

*Project supported by the National Natural Science Foundation of China (Grant Nos. 51876184, 51706193, and 51776037), the National Natural Science Foundation of China–NSAF (Grant No. U1530260), the China Postdoctoral Science Foundation (Grant No. 2017M621835), the Natural Science Foundation of the Jiangsu Higher Education Institutions of China (Grant No.17KJB470014), and Jiangsu Planned Projects for Postdoctoral Research Funds, China (Grant No. 1701188B).

†Corresponding author. E-mail: liuxd@yzu.edu.cn

© 2019 Chinese Physical Society and IOP Publishing Ltd

reveal the underlying physics of droplet behavior under external flow in a microchannel.[20,21] Recently, two- and three-dimensional numerical simulations have been carried out to study the deformation,[22–25] pinch-off,[26,27] and detachment of a single droplet[3,28] in the shear flow. For example, Cho *et al.*[22] found that the dynamic behaviors of the droplets are governed by competition among the drag force, retentive force, lifting force, and body forces (gravity, buoyancy force, *etc*.). The numerical study by Gupta *et al.*[29] indicated that the deformation of the droplet is intensified with increasing capillary number, Reynolds number, and droplet size. Moreover, Kang *et al.*[30] investigated the motions of an immiscible droplet subjected to the continuous phase under gravity. The results showed that the displacement of the droplet is affected not only by the contact angle, Bond number, and droplet size, but also by the density and viscosity ratios of the droplet to the continuous phase. Moreover, the droplet can be detached from the microchannel substrate more easily under smaller body forces.

In summary, the dynamic behavior of a droplet adhered to the substrate of a micro-channel have attracted great attention during the past decades. However, the majority of the available studies focus on the individual dynamics of a single droplet with no interaction with others. However, it must be pointed out that, in the real applications, the interaction between droplets under the external fluid is also common. For instance, Chen *et al.*[31] observed the coalescence of two droplets in a microchannel, after which the surface energy is released and the coalescent droplet undergoes an oscillation process. Nevertheless, the efforts dedicated to exploring the coalescing process and especially the following dynamic behaviors of the coalescent droplet under the external flow in a microchannel are still limited. In particular, the hydrodynamics underlying the droplets coalescing and the following motion still needs to be fully understood. In this context, we performed a three-dimensional numerical simulation to investigate the binary coalescence of droplets under air flow in a hydrophobic microchannel. Accordingly, the droplets coalescing and the following dynamic behavior of the coalescent droplet is analyzed, and the corresponding underlying hydrodynamics is clarified.

2. Mathematical model

As shown in Fig. 1, in order to investigate the hydrodynamic binary coalescence of droplets under air flow in a hydrophobic microchannel, a three-dimensional rectangular microchannel with a length of 2000 μm and square cross-section 100 μm × 100 μm is chosen as the computational domain. Two stationary water droplets with an equal initial radius of 12.5 μm are initially patched in the center line on the substrate of the microchannel along the x direction. The initial center distance between these two droplets is $\Delta d = 50$ μm, and the initial distance between the microchannel inlet and the center of the upstream droplet is $l_0 = 300$ μm. Under the air flow in a microchannel, two droplets experience sliding, coalescing and the following dynamic behavior are discussed later.

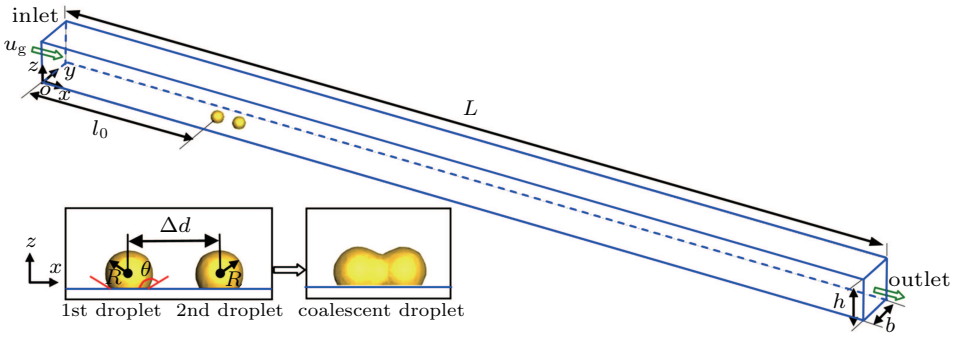


Fig. 1. Schematic diagram of the computational domain.

Table 1. Geometry parameters of the computational domain.

L/μm	b/μm	h/μm	l_0/μm	Δd/μm	R/μm	D/μm	θ/(°)
2000	100	100	300	50	12.5	100	150

2.1. Governing equations

Considering the Knudsen number in the current study, $Kn = \lambda/D = 6.11 \times 10^{-4}$ (where λ is the mean free path of the air molecule, and D is the microchannel's hydraulic diameter in this study), is much smaller than 0.001,[32] the air flow in the current study can be regarded as the continuous flow. Herein, in order to numerically represent the temporal and spatial evolutions of gas–liquid interface, a three-dimensional unsteady numerical model is established based on the volume of fluid (VOF) method, treating the droplets and external continuous phases as incompressible fluids. The volume fraction of phase in each cell is represented by the volume fraction α; the total volume fractions of all phases in the computational domain are equal to unity, *i.e*.,

$$\alpha_l + \alpha_g = 1. \tag{1}$$

In a gas–liquid two-phase flow, in regard to the volume fraction of the liquid phase α_l, and the volume fraction of the

gas phase $\alpha_{\rm g}$, there are three following possible conditions:

$$\begin{array}{ll} \alpha_l = 1, & \text{cell is filled with liquid phase;} \\ 0 < \alpha_l < 1, & \text{cell is partially filled with liquid phase;} \\ \alpha_l = 0, & \text{cell is filled with gas phase.} \end{array} \tag{2}$$

Furthermore, in order to track the gas–liquid interface in the computational domain, the volume fractions of liquid and gas can be respectively described as

$$\frac{\partial \alpha_{\rm l}}{\partial t} + \boldsymbol{v} \cdot \nabla \alpha_{\rm l} = 0, \tag{3}$$

$$\frac{\partial \alpha_{\rm g}}{\partial t} + \boldsymbol{v} \cdot \nabla \alpha_{\rm g} = 0. \tag{4}$$

Assuming that the current process occurs under a fixed temperature of 20 °C with no heat transfer, the continuity and momentum governing equations[33–36] of the gas–liquid two-phase flow are correspondingly given by Eqs. (5) and (6)

$$\nabla \cdot \boldsymbol{v} = 0, \tag{5}$$

$$\rho \left(\frac{\partial \boldsymbol{v}}{\partial t} + \nabla \cdot (\boldsymbol{v}\boldsymbol{v}) \right) = -\nabla p + \nabla \cdot [\mu (\nabla v + \nabla v^{\rm T})] + \rho \boldsymbol{g} + \boldsymbol{F}_{\rm vol}, \tag{6}$$

where $\boldsymbol{v}$ is the velocity vector, ρ is the mixture density (given by Eq. (7)), p is pressure, μ is the mixture viscosity (given by Eq. (8)), $\boldsymbol{g}$ is gravitational acceleration, and $\boldsymbol{F}_{\rm vol}$ is the body face representing the interfacial tension.

The material properties (*e.g.*, density and viscosity) in each cell are defined as a function of the local phase fraction

$$\rho = \alpha_l \rho_l + \alpha_{\rm g} \rho_{\rm g}, \tag{7}$$

$$\mu = \alpha_l \mu_l + \alpha_{\rm g} \mu_{\rm g}. \tag{8}$$

The continuum surface force (CSF) model proposed by Brackbill *et al.*[37] is adopted to calculate interfacial tension. The interfacial tension in the CSF model is regarded as a body force in Eq. (6), which can be calculated by

$$\boldsymbol{F}_{\rm vol} = \sigma \frac{\rho \kappa_{\rm g} \nabla \alpha_{\rm g}}{0.5 \left(\rho_l + \rho_{\rm g} \right)}. \tag{9}$$

Here, σ is the interfacial tension coefficient, $\nabla \alpha_{\rm g}$ is the normal to the interface, and $\kappa_{\rm g}$ is the free interface curvature, which can be defined as

$$\kappa_{\rm g} = -(\nabla \cdot \hat{n}) = \frac{1}{|n|} \left[\left(\frac{n}{|n|} \cdot \nabla \right) |n| - (\nabla \cdot n) \right], \tag{10}$$

where

$$\hat{n} = \frac{n}{|n|}, n = \nabla \alpha_{\rm g}. \tag{11}$$

2.2. Boundary conditions

The following boundary conditions for the computational domain shown in Fig. 1 are applied for the present simulations.[28]

The fluid mass flux at the inlet is specified using a profile for a fully developed flow through a microchannel.[38] At the outlet, the continuous flow is also fully developed

$$x = 2000\ \mu\text{m}, \quad \frac{\partial u}{\partial x} = 0, \quad \frac{\partial v}{\partial y} = 0, \quad \frac{\partial w}{\partial z} = 0. \tag{12}$$

The no-slip condition is applied to the contact area between the fluid and the wall

$$u_\Gamma = v_\Gamma = w_\Gamma = 0. \tag{13}$$

In conjunction with the no-slip condition, the equilibrium contact angle θ, between the interface and the wall[37] within the framework of the CSF model, is implemented to estimate the effects of wall wettability and adhesion on the fluid interface contacting with the wall in equilibrium.[39–41] The normal to the interface on the wall is represented as

$$\hat{n} = \hat{n}_{\rm w} \cos\theta + \hat{t}_{\rm w} \sin\theta, \tag{14}$$

where $\hat{n}_{\rm w}$ is the unit normal vector and $\hat{t}_{\rm w}$ is the tangential vector to the wall. The local curvature of the surface on the wall is determined by combining the contact angle with the calculated surface normal away from the wall, and the body force term for the interfacial tension is calculated by using this curvature.

2.3. Numerical solution method

By using the control volume finite-difference method, the equations of continuity, momentum, and volume fraction along with the boundary conditions above are numerically solved. The fluid flow in a microchannel is simulated by implementing a laminar model because the Reynolds number of all cases simulated is below 400.[42] The momentum equation is discretized using the second-order upwind scheme and the volume fraction equation is solved by the explicit scheme. The body force weighted scheme is implemented as the pressure interpolation scheme, and the semi-implicit method for pressure linked equations (SIMPLE) algorithm is used for the pressure-velocity coupling. The piecewise linear interface calculation (PLIC)[43] method is applied to reconstruct the gas–liquid interface profile.

In the current simulation, a fixed time step of 1×10^{-6} s is used for 200 time steps at first to refine the profile of original patched droplets. Then, according to the real working condition and computational convergence, the time steps of 5×10^{-6} s–5×10^{-5} s are used to guarantee numerical convergence. By adopting successive under-relaxation to improve the numerical convergence, the Gauss–Seidel iterative method coupled with an algebraic multigrid (AMG) method is used to solve the resulting algebraic equations. The under-relaxation factors implemented in the simulation for pressure, density, body force, and momentum are set to be 0.3.

2.4. Grid sensitivity test

Before the formal numerical simulation, a grid sensitivity test is conducted. Take one case in the present work as an example, figure 2 compares the steady contours of a sliding droplet after binary coalescence under air flow in a microchannel, using four different mesh resolutions. As indicated, the contour of the deformed sliding droplet converges with the increase of the cells. In particular, the droplet deformation contour changes little when the cell number is larger than 6.0×10^5. Taking both the computational efficiency and accuracy, the computational grid with 6.0×10^5 cells is used in the current numerical simulation.

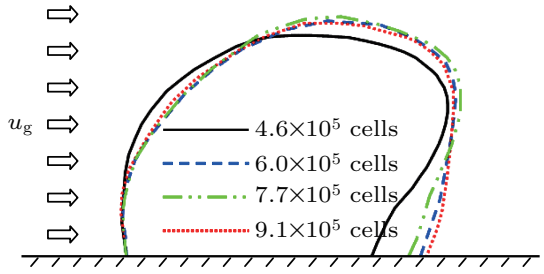


Fig. 2. Contours of the deformed sliding droplet after binary coalescence under different cell numbers ($Re = 185$, $Ca = 0.006713$, and $u_g = 27$ m/s).

2.5. Model validation

To verify that the present mathematical model is reasonable, we use the current model to simulate a typical experimental case by Seevaratnam *et al.*[15] and compare the numerical and the experimental results. The same parameters as the experiment, including droplet size, surface wettability, and contact angle, are used in the model validation. Figure 3 compares the current numerical results with the experimental data obtained in the deforming and detaching processes of a single droplet under air flow. As shown in Fig. 3(a), the time-dependent images are in good agreement with the experimental data. Furthermore, figure 3(b) also compares the numerical results and experimental data on the temporal contact line (CL) evolution, which indicates that the average relative deviation between numerical and experimental results is 5.2%. These positive agreements between experimental data and numerical results verify that the present mathematical model is reliable.

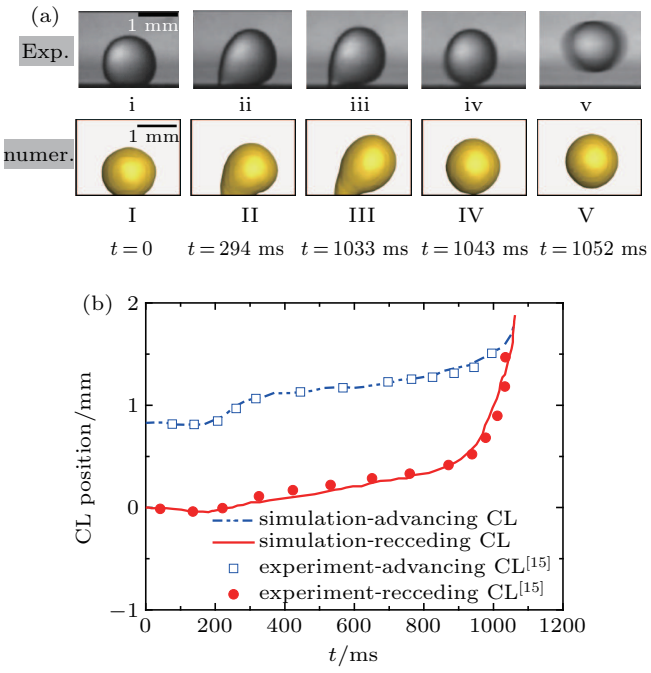


Fig. 3. Comparison of the experiment data[15] and present numerical results on the deforming and detaching processes of a single droplet under air flow ($Ca = 0.0056$): (a) evolution of droplet contours; (b) evolution of the advancing and receding contact lines.

3. Results and discussion

In this study, we focus on the evolution of coalescing and the subsequent behaviors of two droplets under air flow in a hydrophobic microchannel with a contact angle of 150°. Water and air, with a density of 998.2 kg/m^3 and 1.225 kg/m^3, and viscosity of 1.003×10^{-3} kg/m·s and 1.79×10^{-5} kg/m·s, are used as the droplet's fluid and continuous phases in the present calculations. The interfacial tension between them is 0.072 N/m. Two regimes, sliding after droplet coalescence and detaching after droplet coalescence, are obtained under different conditions.

3.1. Forces acting on the droplet

In the presence of the air flow, the droplets adhering to the microchannel wall undergo three kinds of force, *i.e.*, hydrodynamic force, interfacial tension, and gravity. The hydrodynamic force acting on a droplet is induced by viscous stress and pressure gradient arising from air flow, which can be decomposed into the drag force $\boldsymbol{F}_\mathrm{D}$ along the flow direction and the lift force $\boldsymbol{F}_\mathrm{L}$ in the direction of the surface normal, as shown in Fig. 4. The corresponding calculating formulas of $\boldsymbol{F}_\mathrm{D}$ and $\boldsymbol{F}_\mathrm{L}$ are determined by integrating the pressure p and viscous stresses τ over the droplet surface S:

$$\boldsymbol{F}_\mathrm{D} = \boldsymbol{F}_{\mathrm{D},p} + \boldsymbol{F}_{\mathrm{D},v} = \boldsymbol{e}_x \cdot \left(\int_S -p\boldsymbol{e}_n \mathrm{d}S + \int_S \boldsymbol{n}\cdot\tau \mathrm{d}S \right), \quad (15)$$

$$\boldsymbol{F}_\mathrm{L} = \boldsymbol{F}_{\mathrm{L},p} + \boldsymbol{F}_{\mathrm{L},v} = \boldsymbol{e}_z \cdot \left(\int_S -p\boldsymbol{e}_n \mathrm{d}S + \int_S \boldsymbol{n}\cdot\tau \mathrm{d}S \right), \quad (16)$$

where $\boldsymbol{e}_x$ and $\boldsymbol{e}_z$ are unit vectors in the x and z directions, respectively, and $\boldsymbol{n}$ denotes the unit normal vector to the surface of a droplet. The first term is the pressure force, and the second term is the viscous force. Notably, analytically speaking, $\boldsymbol{F}_\mathrm{D}$ and $\boldsymbol{F}_\mathrm{L}$ are both positively correlated with the hydrodynamic inertia of the external air flow.

In previous studies, the interfacial tension acting on a droplet produces the adhesion force $\boldsymbol{F}_\mathrm{a}$, which originates from

the molecular interaction between the droplet and solid wall. This adhesion force opposes the droplet motion driven by the air flow. As shown in Fig. 4, the component forces, $\boldsymbol{F}_{a,x}$ and $\boldsymbol{F}_{a,z}$ resist against the droplet sliding and vertical motions, respectively. As stated in Ref. [44], the adhesion force is determined by interfacial tension, contact angles, and the geometric shape of the contact line. In theory, the calculating formula of the adhesion force can be given by integrating the interfacial tension acting in the direction of the local contact angle around the three-phase contact line.[44] However, in practice, it is difficult to accurately determine the direction of the local contact angle according to the numerical simulation results. Although some theoretical predictions are utilized to obtain the tangential (x direction) and normal (z direction) component forces, *i.e.*, $\boldsymbol{F}_{a,x}$ and $\boldsymbol{F}_{a,z}$, by means of different simplified contact angle models,[11,22] these models are still waiting to be verified. In this context, the adhesion force will not be quantitatively characterized in this study. However, it has been well acknowledged that the value of $\boldsymbol{F}_a$ is positively correlated with interfacial tension and contact area between droplet and substrate.[44]

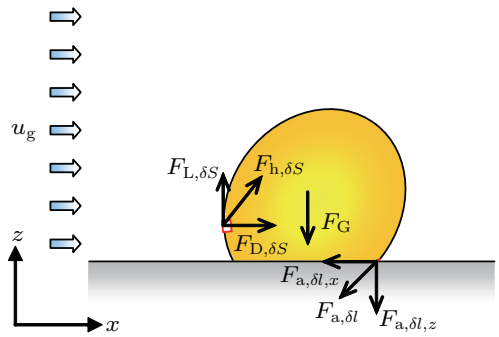


Fig. 4. Schematic diagram of the forces acting on a liquid droplet under the external flow on a hydrophobic wall.

The third kind of force acting on the droplet is gravity $\boldsymbol{F}_G$. For a droplet on the substrate under air flow, the gravitational effect depends on Bond number, $Bo = 4(\rho_l - \rho_g)gR^2/\sigma$, which characterizes the ratio of gravity to interfacial tension. Herein, bond number with the magnitude of 10^{-4} is much less than unity. It implies that, in our study, gravity has little effect on the dynamic behavior of droplets with respect to the interfacial tension.

The force analysis reveals that the hydrodynamic force and interfacial tension are key factors for droplet motion under air flow. When the hydrodynamic force overcomes the adhesion force induced by interfacial tension and the low gravity, the droplet would slide on the substrate ($|\boldsymbol{F}_D| > |\boldsymbol{F}_{a,x}|$) or even totally lift off ($|\boldsymbol{F}_L| > |\boldsymbol{F}_{a,z}| + |\boldsymbol{F}_G|$).

To investigate the effects of the hydrodynamic force and interfacial tension, two corresponding dimensionless parameters are introduced, *i.e.*, Weber number (*We*) and Reynolds number (*Re*).[45,46] The Weber number characterizes the ratio of inertial force to interfacial tension, which is defined as

$$We = \frac{\rho_g u_g^2 d}{\sigma}, \tag{17}$$

where ρ_g is the air density, u_g is the velocity of air, d denotes the diameter of droplet, and σ denotes the interfacial tension coefficient. The Reynolds number characterizes the ratio of inertial force to viscous force

$$Re = \frac{\rho_g u_g D}{\mu_g}, \tag{18}$$

where μ_g is the air viscosity and D is the microchannel's hydraulic diameter.

3.2. Droplet coalescence followed by sliding motion

3.2.1. Dynamic behavior of droplet coalescence followed by sliding motion

When *Re* and *We* are relatively small, the coalescent droplet slides towards the outlet of microchannel afterwards, as shown in Fig. 5, which presents the temporal evolution of hydrodynamic information during the coalescence process followed by the sliding motion. It can be seen from Fig. 5(a) that, when the drag force overcomes the tangential (x direction) component of adhesion force, *i.e.*, $|\boldsymbol{F}_D| > |\boldsymbol{F}_{a,x}|$, the droplets start to slide along the substrate of the microchannel towards the outlet. Due to the shelter of the upstream droplet (first droplet), the downstream droplet is subjected to the wake zone of the upstream one, and thus undergoes smaller drag force from the air stream. Therefore, the downstream droplet gets a lower sliding speed than the upstream one. As a result, the upstream droplet gradually catches up with the downstream one until coalescence occurs. After coalescence, the merged droplet continues to slide downstream to the microchannel outlet, accompanied by the gradually decaying oscillation of its profile. Finally, it moves at a constant speed and achieves a steady shape slightly tilted to the microchannel outlet.

The detailed velocity fields and pressure contours from the front view and top view during coalescence and sliding motion are presented in Fig. 5(b). As shown in Fig. 5(b), at $t_{s,1}$, droplets begin to contact with each other and a liquid bridge forms between them. The pressure in the liquid bridge at $t_{s,1}$ is lower than the pressure in both ends of the dumbbell-shaped coalescent droplet, as shown in Fig. 5(b) II and IV. Accordingly, liquid from the ends flows into the liquid bridge under the pressure difference. Due to gradual exhaustion of surface energy released during the coalescence process, the coalescent droplet then undergoes a damped oscillation process. As the oscillation terminates, the shape and movement speed of the coalescent droplet gradually reach steady, implying that a balance occurs between $\boldsymbol{F}_D$ and $\boldsymbol{F}_{a,x}$, as shown at $t_{s,6}$ in Fig. 5.

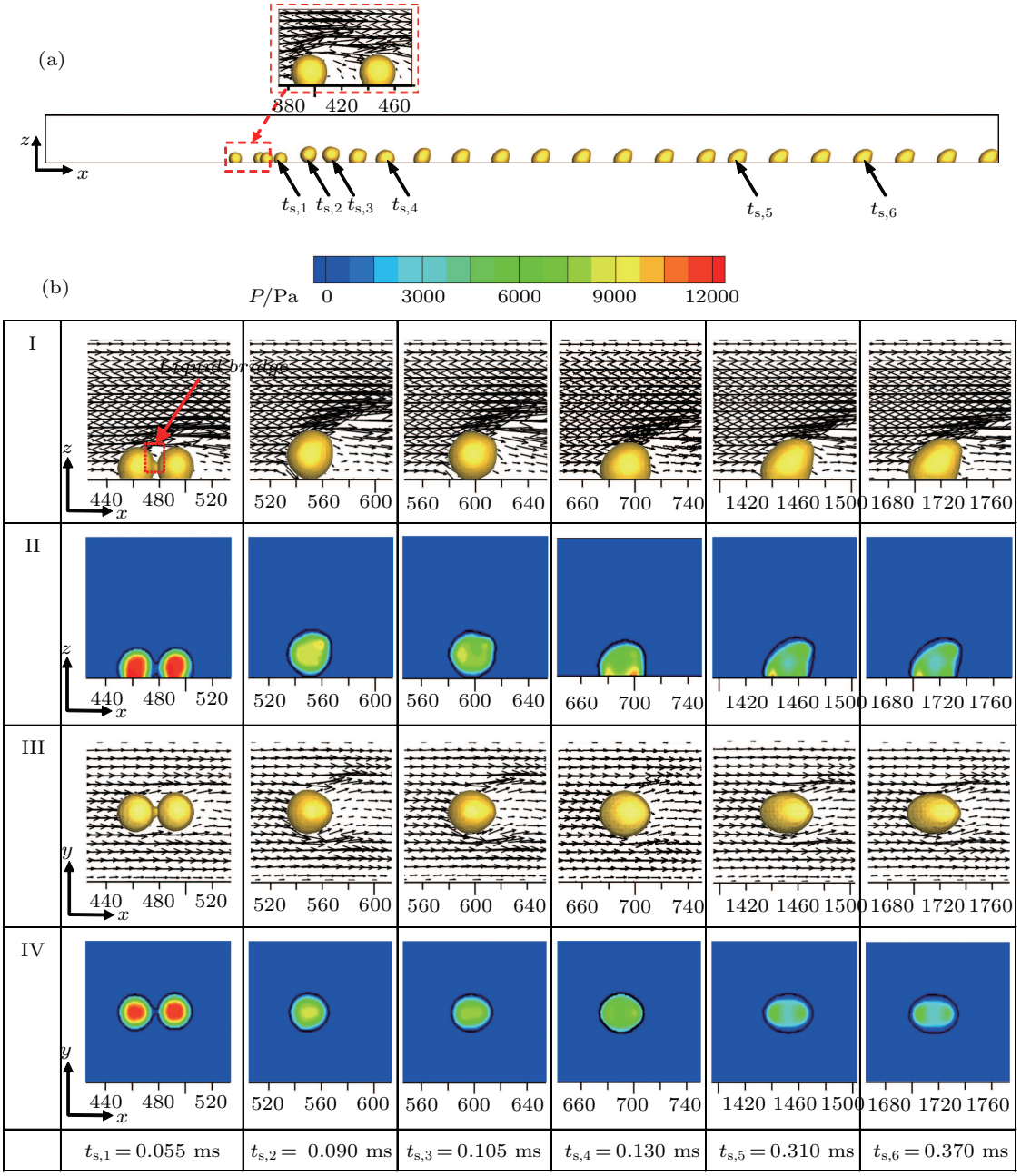


Fig. 5. Spatiotemporal evolution of the droplet's coalescence followed by sliding motion ($Re = 185$, $We = 1.242$): (a) evolution of the motion; (b) evolution of the velocity field and pressure contours at the cross-section of $y = 50$ μm.

3.2.2. Dynamic mechanical analysis of droplet coalescence followed by sliding motion

In order to further understand the dynamic behavior of droplet coalescence followed by sliding motion, the quantitative evolutions of droplet velocity along the main flow direction, the droplet-wall contact area, as well as drag and lift forces on the droplet are presented and discussed in this section.

As a significant concept in kinematics, the evolution of droplet sliding velocity along the main flow direction is presented in Fig. 6. In the beginning, two droplets accelerate from rest under air flow. As mentioned above, due to the shelter of the upstream droplet (first droplet), the downstream droplet (second droplet) moves more slowly. Consequently, the first droplet gradually catches up with the second droplet. At the moment of $t_{s,1}$, the two droplets make contact and merge with each other. Then the merged droplet rapidly accelerates with the shape oscillation until the moment $t_{s,4}$ (see Figs. 5(a) and 6). After this moment, the sliding velocity of the droplet slowly increases to a constant value. This implies that the forces applied on the droplet reach balance.

Based on the force analysis in Subsection 3.1, the sliding motion of a droplet is driven by the drag force from the air. Accordingly, based on Eq. (6), figure 7 provides the corresponding evolution of drag force acting on the droplets. As shown, from the initial time to $t_{s,1}$, the drag force acting on each droplet goes down. This is because the acceleration of the droplet reduces the speed difference between the droplets

and mainstream. Note that, due to the shelter of the upstream droplet, the drag force acting on the second droplet is smaller than that of the first droplet, which is consistent with the greater acceleration of the first droplet than the second one shown in Fig. 6 before $t_{s,1}$. During the stage from $t_{s,1}$ to $t_{s,4}$, the merged droplet experiences a shape oscillation process and thus induces the oscillatory evolution of the drag force. After the moment of $t_{s,4}$, the influence of the shape oscillation decays with time. At the final stage, the drag force acting on the coalescent droplet reaches a steady state. Especially, owing to the bigger windward area, the coalescent droplet gets larger drag force than the droplets before the coalescence.

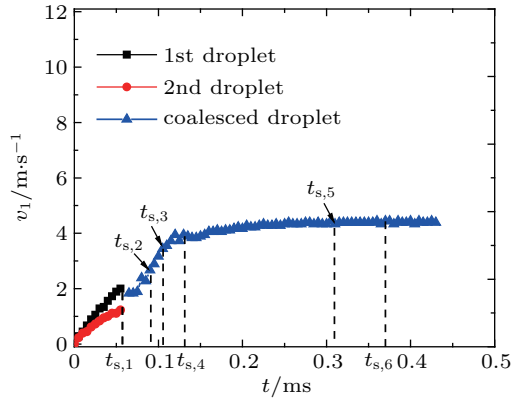


Fig. 6. Evolution of the sliding velocity of droplet along the main flow direction ($Re = 185$, $We = 1.242$).

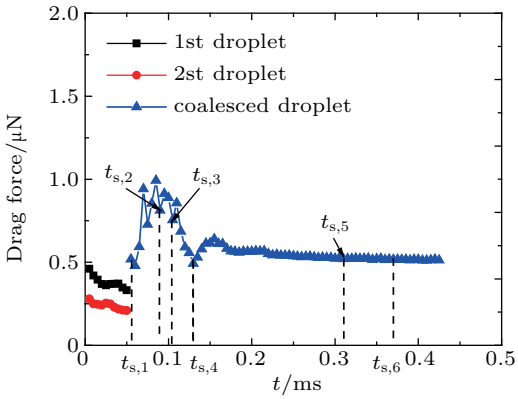


Fig. 7. Evolution of the drag force acting on the droplets ($Re = 185$, $We = 1.242$).

Except for the drag force for driving the droplet movement in the x direction, the applied forces acting in the z direction is another important factor that governs the subsequent lift motion after the droplet coalescence. Herein, the evolutions of the droplet barycenter motion in the z direction and the droplet–wall contact area are taken as key parameters to affect the droplet lift motion, which are closely related to the adhesion and lift forces on the droplet. As shown in Fig. 8(a), the droplet–wall contact area A slightly varies before two droplets coalesce. At the initial merging stage, the contact area of the merged droplet with the substrate is double that of the droplets before the coalescence at $t_{s,1}$. After that, the contact area fluctuates sharply with the oscillation of the merged droplet from $t_{s,1}$ to $t_{s,4}$. Particularly, around the moment of $t = 0.1$ ms, the merged droplet mostly detaches from the wall twice at $t_{s,2}$ and $t_{s,3}$. However, the lift force at these two moments cannot overcome the adhesion force along the direction of the substrate normal. Afterwards, the contact area increases sharply quickly and reaches a steady value during the final steady sliding motion. Figure 8(b) presents the evolutions of the droplet barycenter motion in the z direction during the whole coalescence process. As indicated, the variation in the height of the droplet barycenter is opposite to the contact area. Note that, it also goes through a period of fluctuation from $t_{s,1}$ to $t_{s,4}$, during which it exceeds the radius of the merged droplet for a while corresponding to the periods around $t_{s,2}$ and $t_{s,3}$ with minimum contact area.

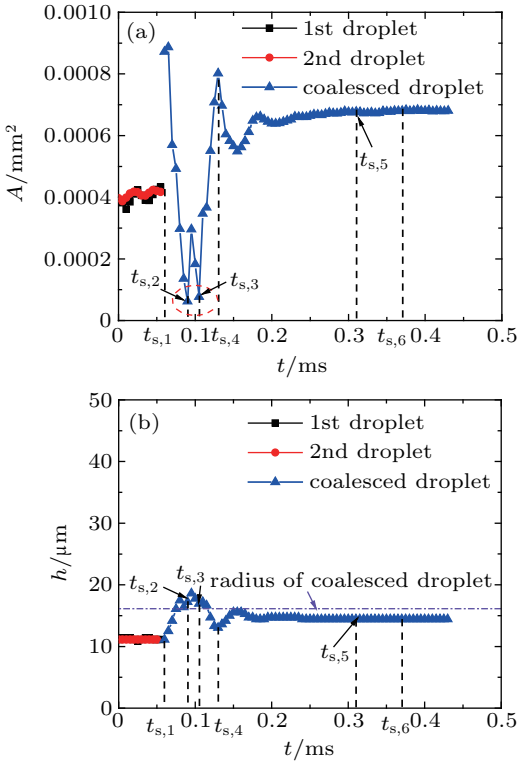


Fig. 8. Evolutions of the droplet–wall contact area and droplet barycenter motion in the z direction ($Re = 185$, $We = 1.242$).

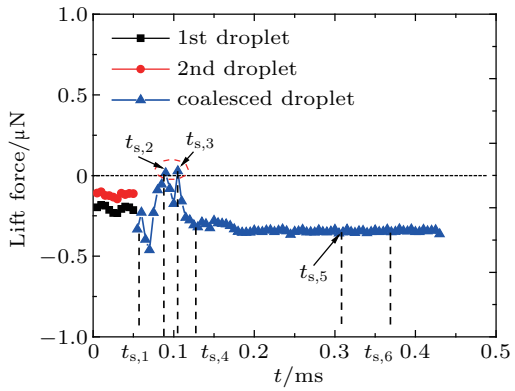


Fig. 9. Evolution of the lift force acting on the droplets ($Re = 185$, $We = 1.242$).

In addition, the detailed evolution of the lift force presented in Fig. 9 provides a support to further understand

droplet coalescence followed by sliding motion. It can be seen that the lift force acting on the droplet is almost negative, except for two moments at $t_{s,2}$ and $t_{s,3}$. This implies that in this case, the lift force always resists the detachment of the droplet other than $t_{s,2}$ and $t_{s,3}$. But even if these distinctive positive values correspond to the moments with the minimum contact area in Fig. 8(a) (*i.e.*, the minimum adhesion force in the z direction), the positive lift forces are too small to produce the detachment of the coalescent droplet.

3.3. Droplet coalescence followed by detachment of coalescent droplet

3.3.1. Dynamic behavior of droplet coalescence followed by detaching motion

When *Re* and *We* are large, the coalescent droplet slides only for a very short time and detaches from the substrate of the microchannel afterwards, as shown in Fig. 10. It can be seen that two droplets contact with each other and start merging at $t_{d,1} = 0.050$ ms. Then at $t_{d,3} = 0.100$ ms, the sliding merged droplet begins to detach from the substrate. Note that, at the contacting moment, the merging droplet experiences an oscillation process, which leads to large deformation of the droplet (see $t_{d,2} = 0.070$ ms). Especially, It can be seen from the detachment at $t_{d,3} = 0.100$ ms that, owing to the near-wall effect, the velocity of the air below the droplet is lower than that around the merged droplet, especially than that at the top of the droplet. Therefore, the static pressure below the droplet near the microchannel bottom is higher than the other regions, which produces an aerodynamic lifting pressure difference for propelling the detachment of the merged droplet.

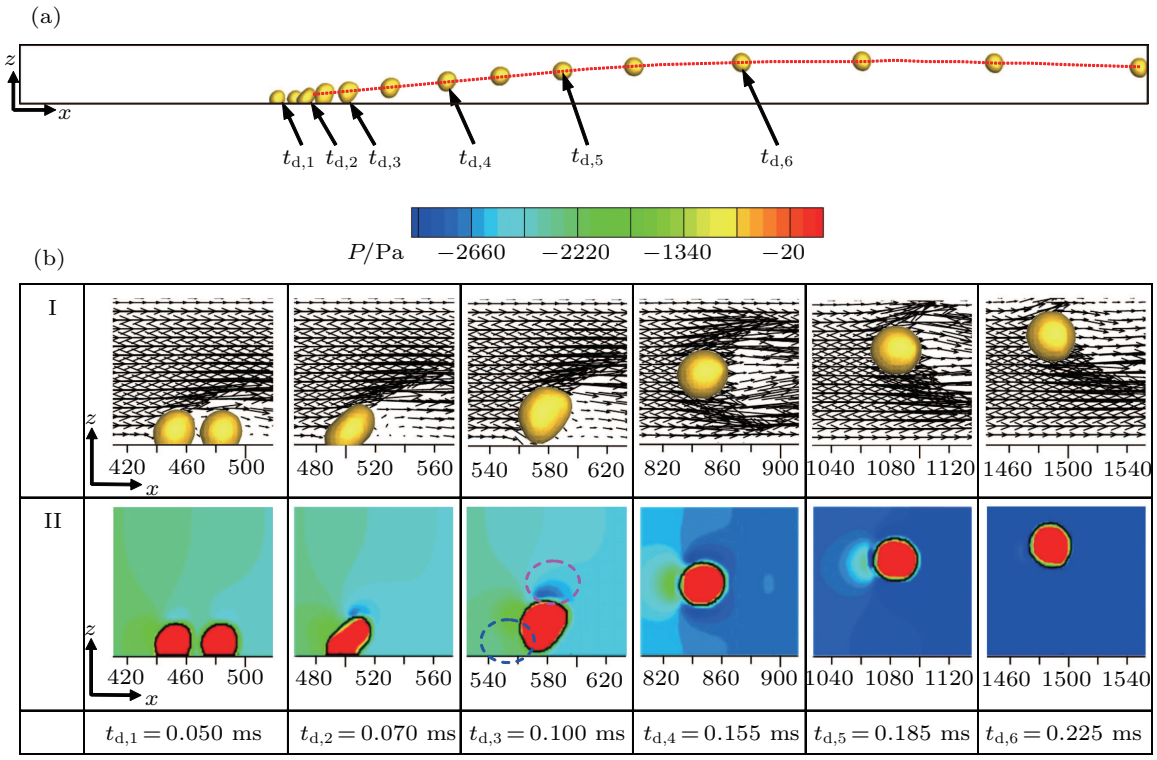


Fig. 10. Spatiotemporal evolution of the droplets coalescence followed by detachment of coalescent droplet (*Re* = 185, *We* = 2.484): (a) evolution of the motion; (b) evolution of the velocity field and pressure contours at the cross-section of $y = 50$ μm.

3.3.2. Dynamic mechanical analysis of droplet coalescence followed by detaching motion

Similar to the previous discussions, the quantitative evolution of droplet velocity along the main flow direction, the droplet–wall contact area, and the drag and lift forces acting on the droplet are presented to understand the behavior of droplets, especially during the detaching period.

Figure 11 presents the evolution of droplet velocity along the main flow direction. Similar to the cases discussed in Subsection 3.2, the droplet accelerates before and after coalescence under air flow. What makes it different is that the merged droplet starts to detach from the substrate of the microchannel at $t_{d,3} = 0.100$ ms. Afterwards, there exists no adhesion force resisting the droplet movement along the main flow direction. Therefore, the velocity of the merged droplet increases monotonously after the droplet detachment (see Fig. 11).

Figure 12 provides the evolution of the drag force acting on the droplets. Before the detaching moment of $t_{d,3} = 0.100$ ms, the variations of the drag forces on two initial droplets are similar to those discussed in Subsection 3.2. Nevertheless, after the detaching moment, the drag force slightly increases and then turns to a drop after $t_{d,4}$ until it reaches a steady value. As shown in Figs. 10(a) and 10(b) I, this

phenomenon is attributed to the droplet deformation, especially the change of droplet position in the main flow, which leads to a different external flow state around the droplet. In addition, the evolutions of the droplet–wall contact area and droplet barycenter motion in the z direction are given in Fig. 13. As shown in Fig. 13(a), after the contacting moment at $t_{d,1} = 0.050$ ms, the droplet–wall contact area slightly increases for a while and then goes down sharply until it is equal to zero at $t_{d,3} = 0.100$ ms when the droplet lifts off. After the detachment of the droplet at $t_{d,3} = 0.100$ ms, the droplet barycenter rapidly rises (see Fig. 13(b)).

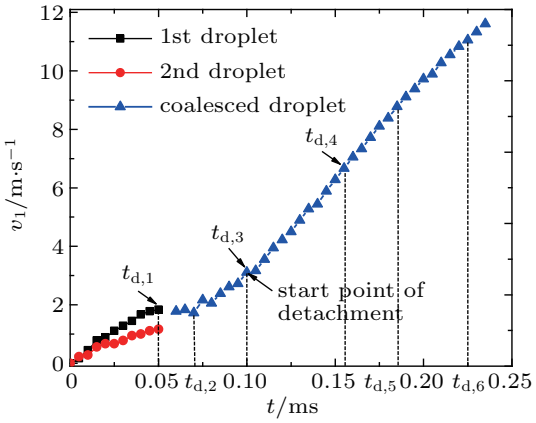


Fig. 11. Evolution of sliding velocity of a droplet along the main flow direction ($Re = 185$, $We = 2.484$).

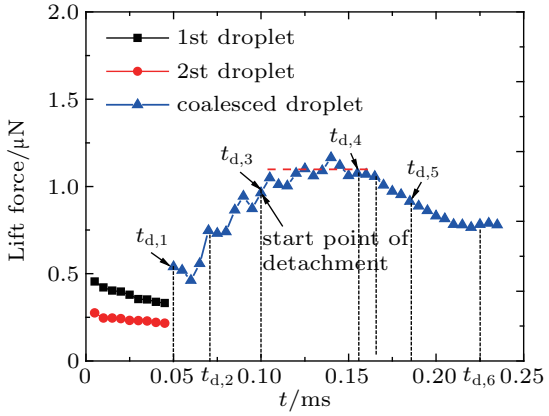


Fig. 12. Evolution of the drag force acting on the droplets ($Re = 185$, $We = 2.484$).

In order to elucidate detachment of the merged droplet, figure 14 presents the detailed variation of the lift force imposed on the droplet. As shown, the lift force remains negative even before the detaching moment at $t_{d,3} = 0.100$ ms. Only when the merged droplet starts to lift off, it changes to positive, which contributes to the detachment of the droplet and the following upward motion. This phenomenon raises the question of what drives the droplet lifting off at the start point of detachment against adhesion force component in the z direction. The reason should be the increment in the above-mentioned aerodynamic lifting pressure difference for propelling the detachment of the coalescent droplet.

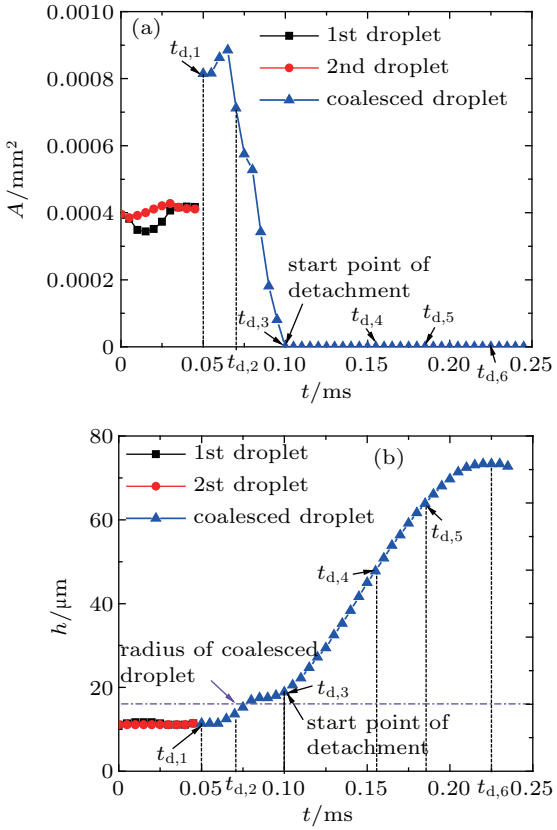


Fig. 13. Evolution of the droplet–wall contact area and droplet barycenter motion in the z direction ($Re = 185$, $We = 2.484$).

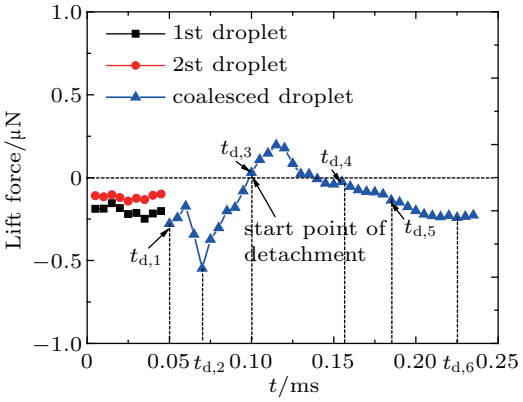


Fig. 14. Evolution of the lift force acting on the droplets ($Re = 185$, $We = 2.484$).

3.4. Phase diagram of regimes

As mentioned above, the competition between the hydrodynamic force and interfacial tension mainly determines the binary coalescence of droplets and the following behaviors of the merged droplet, which can be synthetically characterized by Re and We. Therefore, based on the current numerical results, figure 15 plots the regime distribution depending on Re and We. As indicated in the figure, the detachment after droplet coalescence tends to occur with higher We and Re. Obviously, higher Re means greater inertial forces of the air flow, *i.e.*, greater hydrodynamic forces here, leading to larger lifting forces acting on the droplet. In addition, larger We stands for smaller interfacial tension with respect to the inertial forces, which results in smaller adhesion forces to restrain the droplet.

These factors both contribute to the detachment of the coalescent droplet.

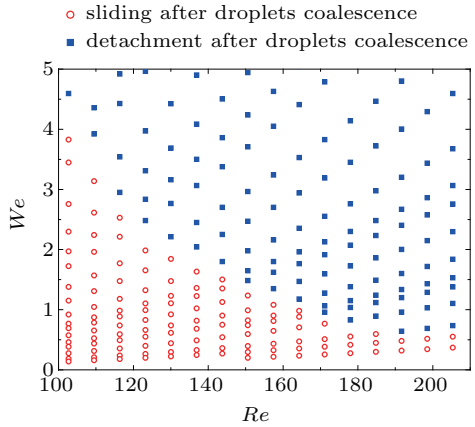


Fig. 15. Phase diagram of the regimes.

4. Conclusion

The hydrodynamic binary coalescence of droplets under convection in a hydrophobic rectangular microchannel is studied using a numerical simulation based on the VOF method. The temporal morphology and motion development during and after the coalescence are presented. Additionally, detailed hydrodynamic information behind the binary coalescence is provided, based on which a dynamic mechanical analysis is conducted to reveal the hydrodynamic mechanisms. The conclusions can be summarized as follows.

(i) Two distinct regimes, coalescence followed by sliding motion and that followed by detaching motion, are identified via the simulation.

(ii) Based on the dynamic mechanical analysis, the sliding motion of a droplet is driven by the drag force and restrained by the adhesion force induced by the interfacial tension along the main flow direction. Similarly, the detachment (*i.e.*, upward motion) of a droplet is driven by the lift force and also restrained by the adhesion force perpendicular to the main flow direction. For coalescence followed by the sliding motion, the lift force acting on the droplet is mostly negative, which mainly resists the detachment of the droplet. While, under coalescence followed by the detaching motion, the lift force becomes positive and contributes to the detachment of the droplet at the start point of droplet lifting off, which is attributed to an aerodynamic lifting pressure difference imposed on the coalescent droplet.

(iii) These two typical regimes can be quantitatively recognized by a regime diagram depending on *Re* and *We*. The higher *Re* and *We* lead to relatively larger lift forces and smaller adhesion forces on the droplet, respectively, both of which are helpful to induce the detachment of the coalesced droplet.

We believe that the current work and results will not only contribute to fully understanding the hydrodynamics underlying the droplet coalescence and the following dynamic behaviors under the external flow in a microchannel, but also be beneficial to the control and optimization of the real processes associated with these phenomena.

References

[1] Sharma M M, Chamoun H, Sarma D S H S R and Schechter R S 1992 *J. Colloid Interface Sci.* **149** 121
[2] Orme M 1997 *Prog. Energy Combust. Sci.* **23** 65
[3] Dimitrakopoulos P and Higdon J J L 1997 *Phys. Fluids* **336** 351
[4] Thompson L 1994 *J. Colloid Interface Sci.* **163** 61
[5] Eckmann D M, Cavanagh D P and Branger A B 2001 *J. Colloid Interface Sci.* **242** 386
[6] Wang J, Gao W, Zhang H, Zou M H, Chen Y P and Zhao Y J 2018 *Sci. Adv.* **4**
[7] Cai Y H, Hu J, Ma H P, Yi B L and Zhang H M 2006 *J. Power Sources* **161** 843
[8] Quan P, Zhou B, Sobiesiak A and Liu Z 2005 *J. Power Sources* **152** 131
[9] Peng Q and Lai M C 2007 *J. Power Sources* **164** 222
[10] Proceedings of ASME 2003 1*st International Conference on Fuel Cell Science, Engineering and Technology*, April 21–23, 2003, Rochester, USA, p. 143
[11] Basu S, Nandakumar K and Masliyah J H 1997 *J. Colloid Interface Sci.* **190** 253
[12] Madani S and Amirfazli A 2014 *Colloids Surf. A* **441** 796
[13] Vananroye A, And P V P and Moldenaers P 2006 *Langmuir* **22** 3972
[14] Akhtar N and Kerkhof P J A M 2011 *Int. J. Hydrogen Energy* **36** 3076
[15] Seevaratnam G, Michel O, Heng J, Ding H, Spelt P and Matar O 2010 *Chem. Eng. Sci.* **65** 4523
[16] Chen Y P, Wu L Y and Zhang C B 2013 *Phys. Rev. E* **87** 013002
[17] Chen Y P, Gao W, Zhang C B and Zhao Y J 2016 *Lab Chip* **16** 1332
[18] Fan J, Wilson M C and Kapur N 2011 *J. Colloid Interface Sci.* **356** 286
[19] Vananroye A, Puyvelde P V and Moldenaers P 2011 *Rheol. Acta* **50** 231
[20] Qi C, Liang L and Rao Z H 2016 *Int. J. Heat Mass Transfer* **94** 316
[21] Sun D K and Bo Z 2015 *Int. J. Heat Mass Transfer* **80** 139
[22] Cho S C, Wang Y and Chen K S 2012 *J. Power Sources* **206** 119
[23] Li Q X, Chai Z H, Shi B C and Liang H 2014 *Phys. Rev. E* **90** 043015
[24] Wang H, Zhang Z Y, Yang Y M, Hu Y and Zhang H S 2008 *Chin. Phys. B* **17** 3847
[25] Wang C Y, Zhang C B, Huang X Y, Liu X D and Chen Y P 2016 *Chin. Phys. B* **25** 108202
[26] Mohammad N H G, Ding H and Spelt P D M 2010 *J. Fluid Mech.* **644** 217
[27] Chen Y P and Deng Z L 2017 *J. Fluid Mech.* **819** 401
[28] Chen F, Hidrovo C, Wang F M, Eaton J and Goodson K 2008 *Int. J. Multiphase Flow* **34** 690
[29] Gupta A K and Basu S 2008 *Chem. Eng. Sci.* **63** 5496
[30] Kang Q J, Zhang D X and Chen S Y 2002 *Phys. Fluids* **14** 3203
[31] Chen Y P, Shen C Q and Peterson G 2015 *Ind. Eng. Chem. Res.* **54** 9257
[32] Chen X P and Pfender E 1983 *Plasma Chem. Plasma Process.* **3** 97
[33] Chen Y P, Zhang C B, Wu R and Shi M H 2011 *J. Power Sources* **196** 6366
[34] Zhang C B, Chen Y P, Wu L Y and Shi M H 2011 *Energ. Buildings.* **43** 3514
[35] Zhang C B, Chen Y P and Shi M H 2010 *Chem. Eng. Process.* **49** 1188
[36] Chen Y P, Zhang C B, Shi M H and Wu J F 2009 *Int. Commun. Heat Mass Transfer* **36** 917
[37] Brackbill J U, Kothe D B and Zemach C 1992 *J. Comput. Phys.* **100** 335
[38] Taha T and Cui Z F 2004 *Chem. Eng. Sci.* **59** 1181
[39] Dr C T, Dr A L Y and Dr J F F 2007 *Springer Handbook Experimental Fluid Mechanics* (Berlin: Springer) pp. 633–636
[40] Saha A A and Mitra S K 2009 *J. Colloid Interface Sci.* **339** 461
[41] Rosengarten G, Harvie D J E and Cooper-White J 2006 *Appl. Math. Model.* **30** 1033
[42] Chen Y P, Zhang C B, Shi M H and Yang Y C 2010 *AIChE J.* **56** 2018
[43] Youngs D L 1982 *Numerical Methods Fluid Dynamics* (New York: Academic Press) pp. 273–285
[44] Antonini C, Carmona F J, Pierce E, Marengo M and Amirfazli A 2009 *Langmuir* **25** 6143
[45] Zhang C B, Chen Y P, Wu R and Shi M H 2011 *Int. J. Heat Mass Transfer* **54** 202
[46] Wu J F, Shi M H, Chen Y P and Li X 2010 *Int. J. Therm. Sci.* **49** 922